Lawrence Berkeley National Laboratory

LBL Publications

Title

Synthesis and characterization of metastable, 20nm-sized Pna21-LiCoPO4 nanospheres

Permalink

https://escholarship.org/uc/item/1hz2g9r8

Authors

Ludwig, Jennifer

Nordlund, Dennis

Doeff, Marca M

et al.

Publication Date

2017-04-01

DOI

10.1016/j.jssc.2017.01.015

Copyright Information

This work is made available under the terms of a Creative Commons Attribution-NonCommercial-NoDerivatives License, available at https://creativecommons.org/licenses/by-nc-nd/4.0/

Peer reviewed

eScholarship.org Powered by the California Digital Library
University of California

Synthesis and Characterization of metastable 20 nm-sized *Pna*2_1-$LiCoPO_4$ Nanospheres

Jennifer Ludwig,[a] Dennis Nordlund,[b] Marca M. Doeff,[c] and Tom Nilges[a]*

[a]Technical University of Munich, Department of Chemistry, Synthesis and Characterization of Innovative Materials, Lichtenbergstr. 4, 85747 Garching, Germany

[b]Stanford Synchrotron Radiation Lightsource, SLAC National Accelerator Laboratory, 2575 Sand Hill Rd, Menlo Park, CA, 94025, USA

[c]Lawrence Berkeley National Laboratory, Environmental Energy Technologies Division, 1 Cyclotron Rd, Berkeley, CA, 94720, USA

Lithium cobalt phosphate; nanoparticles; solvothermal synthesis; microwave synthesis; phase transitions;
metastable compounds; polymorphism; in situ X-ray powder diffraction; X-ray absorption spectroscopy

ABSTRACT: The majority of research activities on $LiCoPO_4$ are focused on the phospho-olivine with the orthorhombic space group *Pnma*, which is a candidate high-voltage cathode material for Li-ion batteries. In contrast, comparably little is known about the structure–property relations of its metastable modification, which contains tetrahedral [LiO_4], [CoO_4], and [PO_4] units and crystallizes within the space group *Pna*2_1. Herein, we present a simple one-step microwave assisted solvothermal synthesis towards uniform, 15 nm *Pna*2_1-$LiCoPO_4$ nanospheres using ethylene glycol as a solvent. The nanomaterial was fully characterized by X-ray powder diffraction, elemental analysis, scanning electron microscopy, BET surface area analysis, infrared spectroscopy, as well as electrochemical measurements. In contrast to previous reports, the results indicate that the compound, which has the empirical formula $Li_{0.95}Co_{1.05}PO_4$, is non-stoichiometric. The combined analytical approach allows for a structure redetermination, which implies a disordered cation substructure with Li/Co mixing on the Li positions. Furthermore, Co *L*-edge X-ray absorption spectroscopic data, which confirm the tetrahedral coordination of the Co^{2+} ions in the structure, are presented for the first time. Comprehensive studies of the thermal stability using thermogravimetric analysis, differential scanning calorimetry, and temperature-dependent *in situ* X-ray powder diffraction reveal that the phase shows a more complex behavior upon heating than previously assumed, involving several phase transitions: a disorder–order transition within the *Pna*2_1 structure at 202 °C, a phase transition to olivine-type *Pnma*-$LiCoPO_4$ at 527 °C, and a partial and reversible transformation back to the initial *Pna*2_1 structure above 800 °C. Furthermore, it is shown that these transitions strongly depend on the atmosphere and the particle size.

INTRODUCTION

Since their commercialization in 1991 by Sony,[1] Li-ion batteries have become a key technology in portable electronics and electric vehicles. To increase specific energies in order to meet future demands, current research activities focus on cathode materials. Particular attention has been given to cathode materials which operate at significantly higher voltage than commercial materials (*e.g.* spinels, lithium-rich layered oxides), as well as new compounds. A potential candidate is the high-voltage cathode material $LiCoPO_4$. Three polymorphs with orthorhombic crystal structures have been reported.

The most common and widely investigated olivine-type $LiCoPO_4$ crystallizes in the space group *Pnma*.[2] The structure consists of two types of polyhedra, [CoO_6] octahedra and [PO_4] tetrahedra, which form a three-dimensional network. The Li^+ ions are located in channels along the [010] and [001] directions. Since the first report by Padhi and co-workers[3] in 1997, intensive efforts[4-6] have been undertaken to optimize the electrochemical performance of the material, which is redox active at ~4.8 V vs. Li/Li^+.[7] Recently, we have reported[8] a facile, one-step microwave-assisted solvothermal (MWST) route towards high-performance $LiCoPO_4$

hexagonal platelets using a mixed 1:1 (v:v) water/ethylene glycol (EG) solvent. The optimized material delivers a specific capacity of 137 mAh/g and an energy density of 658 Wh/kg, which is one of the best performances reported to date.

A high-pressure modification (6 GPa, 1173 K), which exhibits a *Cmcm* symmetry and is isostructural to Na_2CrO_4 was reported by Amador *et al.*[9] in 2009. Like the *Pnma* structure, the compound features a framework of [CoO_6] and [PO_4] units, with Li ions occupying tetrahedral sites which are not interconnected. Recently, Kreder *et al.*[10] demonstrated the low-temperature MWST synthesis and studied the electrochemical properties of the compound, which has an irreversible redox potential of ~4.3 V and an initial discharge capacity of only 6 mAh/g. *In situ* studies on the thermal stability, the magnetic properties, and an alternative polyol synthesis pathway at ambient pressure were also reported by our group.[11]

A third metastable polymorph, which adopts a δ_1-$LiZnPO_4$-like structure in $Pn2_1a$ symmetry, was experimentally reported and characterized by Jaehne *et al.*[12] in 2013 and later by Kreder and co-workers[10]. Unlike the other two polymorphs, the 3D framework exhibits only tetrahedral [PO_4] and [CoO_4] building units with no direct Li channels. The reported crystal structure solutions, however, showed issues regarding the occupancy factors of the Li positions as well as high reliability factors. The groups observed different thermal stabilities for their $Pna2_1$ materials upon heating in an argon atmosphere. Whereas Jaehne *et al.*[12] reported that the compound irreversibly transforms to the thermodynamically stable, olivine-type *Pnma*-$LiCoPO_4$ in an exothermic process at 221 °C, Kreder *et al.*[10] stated that the transition is endothermic and occurs at 340 °C. The reasons for these contradictory observations remained unclear. The redox potential of 4.95 V for $Pna2_1$-$LiCoPO_4$ is the highest of the three $LiCoPO_4$ modifications, which makes it a suitable candidate for high-energy density applications. However, the electrochemical performance has been reported to be poor, with capacities of 27 mAh/g[12] and 33 mAh/g[10] being reached, which is only 16% and 20% of the theoretical capacity of 167 mAh/$g_{LiCoPO4}$. It was suggested that the applicability might be improved by particle size control in order to overcome kinetic limitations.

Based on our work on other $LiCoPO_4$ polymorphs,[8, 11] we herein present a simple microwave-assisted solvothermal approach towards nanostructured $Pna2_1$-$LiCoPO_4$ The structure–property relations of the material were investigated using X-ray powder diffraction, elemental analysis, scanning electron microscopy, BET surface area analysis, infrared spectroscopy, as well as electrochemical measurements. A redetermination of the crystal structure allows further insights into the material properties, and elucidates the reasons for the reportedly poor electrochemical behavior. Co *L*-edge soft X-ray spectroscopic data are reported for the first time and confirm the structure solution. The thermal stability is thoroughly investigated using thermogravimetric analysis, differential scanning calorimetry, and temperature-controlled *in situ* X-ray powder diffraction studies. It is revealed that the phase undergoes several phase transitions, which were not observed in previous studies[10, 12] using *ex situ* techniques.

EXPERIMENTAL SECTION

Microwave-assisted solvothermal (MWST) synthesis

$Pna2_1$-$LiCoPO_4$ was obtained from a modified microwave-assisted solvothermal (MWST) process as reported previously.[8] 22.5 mmol LiOH • H_2O (Bernd Kraft, ≥ 99.0%), 7.5 mmol $CoSO_4$ • 7 H_2O (Chempur, 99%), 7.5 mmol H_3PO_4 (AppliChem, Ph. Eur., 85 wt.% solution), and 0.075 g ascorbic acid reductive (Alfa Aesar, 99+%) were dissolved in 30 mL ethylene glycol (EG, VWR AnalaR NORMAPUR, 99.9%). The red violet suspension (pH = 5.5) was stirred vigorously for 20 min and then transferred into PTFE/TFM reaction vessels (V = 75 mL; HTV-75, MLS GmbH). An Ethos One microwave system (MLS GmbH) equipped with an MR-8 HT high-temperature rotor was used for the synthesis, which was performed at 250 °C for 30 min under continuous stirring and a maximum power of 600 W. The microwave irradiation was adjusted automatically by the T660 temperature control unit. The mixtures (pH =5.0–5.5) were naturally cooled down after the reaction. The dark blue precipitate was recovered by filtration, followed by washing several times with deionized water (high-purity water type I, Millipore, 18.2 MΩ·cm; used to remove a highly water-soluble lithium sulfate side phase[8]) and absolute ethanol (VWR AnalaR NORMAPUR, 99.95%). The powder was then dried in air at 150 °C overnight.

Structural, chemical, and physical characterization

X-ray powder diffraction (PXRD) experiments and Rietveld refinement details. A STADI P diffractometer (Mo $K_{\alpha1}$ radiation, λ = 0.70930 Å) equipped with a Ge(111) monochromator and a Dectris MYTHEN DCS 1K silicon solid-state detector was used to collect PXRD data of the ground powder, which was sealed in a 0.5 mm borosilicate glass

capillary (Hilgenberg). The measurement was performed in a 2θ range of 3–60° (PSD step: 0.015°; time/step: 30 s, three ranges, total measurement time: 12 h). The data were calibrated using an external silicon standard. The Jana 2006 software[13] was used to perform a Rietveld refinement of the diffraction pattern, using the structure solution of the homologue δ_1-$LiZnPO_4$ (space group $Pna2_1$; ICSD no. 79537[14]) as a starting model. A Chebyshev polynomial was used for correcting the background, and the axial divergence model[15] for the peak asymmetry. An estimated packing fraction of ~0.6 was applied for absorption correction. General atomic positions as well as the isotropic thermal displacement parameters of Co, P, and O were refined without restraints, whereas the displacement parameters and positions of Li were kept fixed. Furthermore, a slightly disordered Li/Co distribution on the Li position was assumed. The Berar's correction[16] was applied to all refined parameters in order to obtain more realistic standard deviations.

Elemental analysis. The Li, and Co contents of the material was determined by atomic absorption spectroscopy (AAS, Varian AA280FS device), and the P content by photometry (Shimadzu UV-160 device). The C, H, N, and S contents were measured by combustion analysis (Hekatech Euro EA CHNSO instrument).

Scanning electron microscopy (SEM) and energy-dispersive X-ray spectroscopy (EDS). The morphology of the powder was determined using a JEOL JSM-7500F SEM (accelerating voltage: 1 kV, working distance: 8 mm, LEI (lower secondary electron image) detector). EDS analysis was performed with a Noran system S1X system (Thermo Electron Corporation, model 6714A01SUS-SN, accelerating voltage: 15 kV, probe current: 20 µA). The powder was prepared on carbon tape attached to an Al stub for the measurements.

BET surface area analysis. The specific surface area of the material was determined by the Brunauer–Emmett–Teller (BET) method (Quantachrome Autosorb iQ instrument using) nitrogen physisorption after a degassing period of 12 h at 423 K (11 measurement points).

Rheometry. The dynamic viscosities of high-purity water type I (Millipore, 18.2 MΩ·cm), ethylene glycol (VWR AnalaR NORMAPUR, 99.9%), and a 1:1 (v:v) mixture of both were determined at ambient temperature using an MCR 302 Anton Paar Modular Compact Rheometer in parallel plate–plate geometry (PP-50 plate, diameter: 49.991 mm, gap: 0.250 mm). A volume of ~0.5 mL was used for each measurement, and six measurements were performed in a shear rate range of 1–120 s^{-1} (40 measurement points). The average viscosities were determined at a shear rate of 100 s^{-1}.

Fourier-transform infrared (FTIR) spectroscopy. The FTIR spectrum was collected in a wavenumber range of 400–4000 cm^{-1} (132 scans) using a Varian 670 IR FTIR spectrometer equipped with a PIKE GladiATR ATR stage.

Soft X-ray absorption spectroscopy (soft XAS). Co $L_{2,3}$-edge soft XAS measurements were performed at Stanford Synchrotron Radiation Lightsource (SSRL), beamline 8-2. The sample was attached to an Al sample holder using carbon tape. The incident beam was monochromatized using a spherical grating monochromator (SGM). The $L_{2,3}$-edge μ(E) spectra were collected at room temperature under ultrahigh vacuum (10^{-9} Torr) in the total electron yield (TEY) mode, corresponding to probing depths of 2–5 nm.[17] Co_3O_4 and CoO powders were used as references and all spectra are on a common energy scale as in reference [18]. The spectra were normalized to the beam current and the background subtracted. The intensity of the spectra was further normalized to a maximum of 1 for visual comparison. Further experimental details can be found in reference [8].

Electrochemical measurements. The cathode slurries were prepared by mixing 80 wt % $LiCoPO_4$, 10 wt% carbon (Super C65, Timcal), and 10 wt% polyvinylidene difluoride (PVdF, Solvay) binder with *N*-methyl pyrrolidone (NMP) solvent in an agate mortar. The slurries were cast onto carbon-coated Al current collectors (Coveris Advanced Coatings) using a doctor-blade coater. The electrode sheets were dried at 120 °C for 5 h in a vacuum oven (Thermo Scientific) and then calendered (International Rolling Mills device) in order to increase the contact of the active material with the current collector. The electrode sheets were further vacuum dried for 12 h at 120 °C before being transferred into an Ar-filled glove-box (VAC, < 0.1 ppm H_2O, < 0.1 ppm O_2). Circular electrodes with a diameter of 14.3 mm and typical active material loadings of ~4 mg were punched out. CR2032 coin-type cells were assembled using the $LiCoPO_4$-containing cathode, Li foil (Alfa Aesar, 0.75 mm, 99.9 %, metals basis) as anode, a microporous monolayer PP membrane as separator (Celgard 2400, 25 µm), and 1 M $LiPF_6$ dissolved in ethylene carbonate (EC)/diethyl carbonate (DEC) in a ratio of 1:1 (v:v) as electrolyte (Daikin). Charge–discharge cycling was carried out galvanostatically (BioLogic VMP3 potentiostat/galvanostat) between 3.0 V and 5.2 V at C rates of 0.1 C, 0.2 C, 0.5 C, and 1 C for three cycles each, followed by 20 cycles at 0.1 C. Current densities and specific capacities were calculated on the basis of the weight of

active material in the electrode. In order to minimize statistical effects, two cells were tested.

Thermal analysis using temperature-dependent X-ray powder diffraction (PXRD), thermogravimetric analysis (TGA), and differential scanning calorimetry (DSC). Thermal analysis was performed on a Mettler Toledo TGA/DSC 1 STAR system, which allows simultaneous thermogravimetric analysis (TGA) and differential scanning calorimetry (DSC). A specimen weight of ~5 mg was placed in an alumina crucible, and the experiment run in a temperature range of 30–900 °C (heating rate: 10 °C/min) under two different atmospheres, in an argon and synthetic air stream (both 10 mL/min). Note that only the heating cooling cycle could be monitored due to the instrument setup.

The thermal stability was further assessed by temperature-controlled *in situ* PXRD studies on a PANalytical X'Pert Pro diffractometer in Bragg-Brentano geometry (Cu K_α radiation, XCelerator detector, Anton Parr HTK-1200 hot stage, TCU 1000N temperature controller). The sample, which was placed in a corundum flatplate sample holder, was heated up to 900 °C (heating rate: 5 °C/min, increment step: 100 °C) in air and alternatively under Ar. Each temperature was held for 5 min before starting the data collection. The measurements were performed in a 2θ range of 15–70° (step: 0.022°), with the time/step and total measurement time being increased for the measurement using argon due to lower intensities (air: 209.5 s/step, total measurement time: 145.5 h; Ar: 400 s/step, total measurement time: 277 h).

RESULTS AND DISCUSSION

X-ray powder diffraction and crystal structure

Fig. 1 shows the Rietveld fit of the X-ray powder diffraction pattern of the as-prepared powder. No impurities are detected and all reflections can be indexed using the orthorhombic space group $Pna2_1$ (note that the conventional cell setting is used rather than the non-standardized $Pn2_1a$). The broad reflections indicate that the sample is composed of nanoparticles. The particle size cannot be determined by the Scherrer equation because the main signal consists of two reflections, (210) and (011), which are not well-resolved due to the peak width, but could be estimated to be about ~18 nm in diameter. The nanometric nature of the particles is confirmed by SEM/BET analyses discussed later. Using the structure solution of the homologue δ_1-$LiZnPO_4$ (ICSD no. 79537[14]) as a starting model, the structure can be solved with better reliability factors (Table 1), than in previously published results.[10, 12] The tentative refinement of the occupancy on the Li site resulted in a statistical significant value of 124(8)%, indicating that there is partial substitution with Co. An over-occupation of 122% Li was also reported by Jaehne and co-workers,[12] but no Co mixing was assumed. A Co population of 98(2)% was refined for the Co position, which is not significant within the three sigma rule. Hence, it can be inferred that Li/Co mixing appears on the Li site (occupancies: 94.7(9)% Li and 5.3(9)% Co), whereas the Co site is fully occupied (Table S1). The slightly disordered Li/Co distribution is in good agreement with the structure of δ_1-$LiZnPO_4$. To the best of our knowledge, this is the first time structural disorder has been reported for $Pna2_1$-$LiCoPO_4$. The increase in cell volume (334.8(2) Å^3) compared to olivine $LiCoPO_4$ (293.31(2) Å^3)[8] indicates that the compound is less dense. The empirical formula $Li_{0.947(9)}Co_{1.053(9)}PO_4$ is consistent with the composition determined by elemental analysis (Table 2). Note that for simplicity, the compound is further referred to as $Pna2_1$-$LiCoPO_4$ in this work.

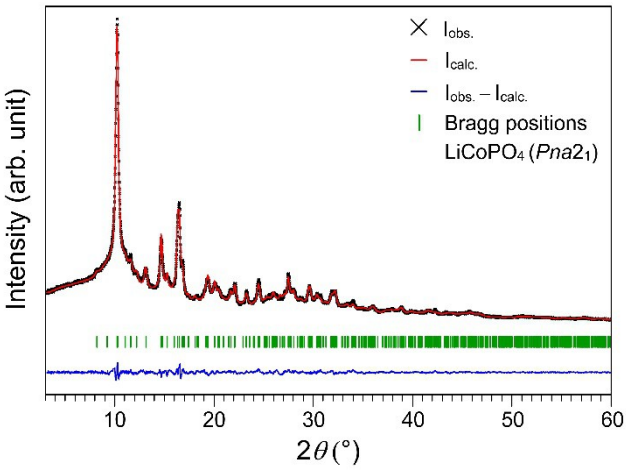

Figure 1. Rietveld fit of the X-ray powder diffraction data (Debye-Scherrer geometry, Mo $K_{\alpha1}$ radiation) of $Pna2_1$-$LiCoPO_4$.

The structure of $Pna2_1$-$LiCoPO_4$ (Fig. 2) exhibits a three-dimensional framework, built from chains of corner-sharing, asymmetric [CoO_4] and [PO_4] tetrahedra (*cf.* interatomic distances, Table S2), and with four-coordinated Li/Co ions on interstitial positions.[12, 14] No direct channels are observed along [001] (Fig. 2c) as they are blocked by [CoO_4] units, and zig-zag channels occur along [100] (Fig. 2a). Distorted six-

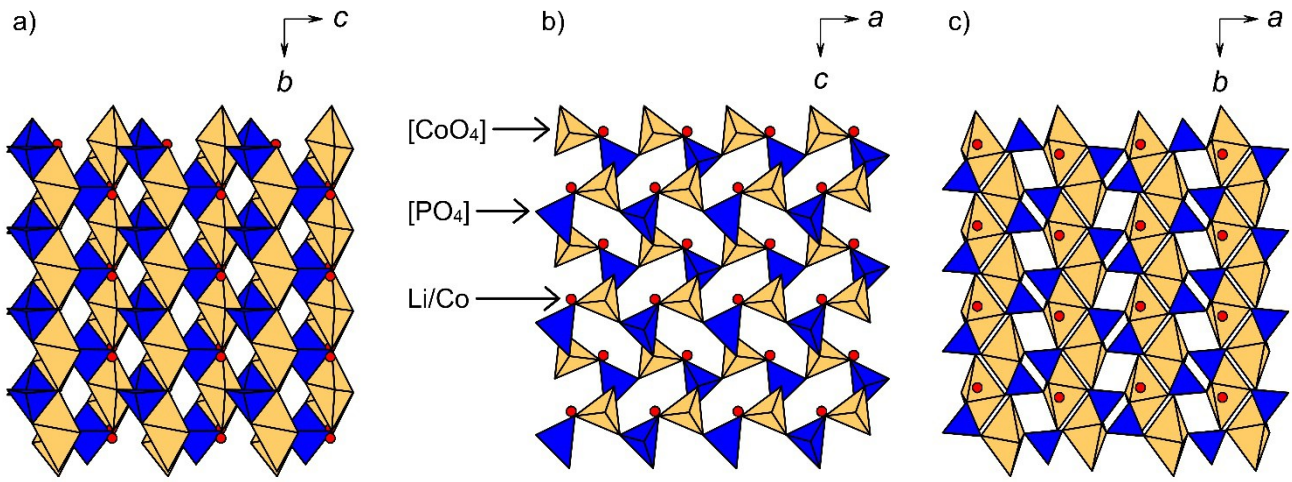

Figure 2. Crystal structure of *Pna*2_1-$LiCoPO_4$ along the three crystallographic axes: (a) [100], (b) [010], and (c) [001]. [CoO_4] tetrahedra are drawn in light orange, [PO_4] tetrahedra in blue, and the mixed site containing 94.7(9)% Li and 5.3(9)% Co in red.

ring channels of alternating [CoO_4] and [PO_4] units are observed along [010] (Fig. 2b), in which the Li/Co ions are located. Despite the channels, however, Li-ion transport is expected to be very limited due to the Li/Co mixing on the Li sites, with Co ions blocking the pathways.

Table 1. Cell parameters of *Pna*2$_1$-$LiCoPO_4$ (*Z* = 4, *T* = 298 K) as refined from X-ray powder diffraction data[a]

Empirical formula	$Li_{0.947(9)}Co_{1.053(9)}PO_4$
M_r (g·mol^{-1})	163.6
Crystal system	orthorhombic
Space group (No.)	*Pna*2$_1$ (33)
Z	4
a (Å)	10.035(4)
b (Å)	4.967(2)
c (Å)	6.716(2)
V (Å^3)	334.8(2)
F(000)	308
ρ (calcd) (g·cm^{-3})	3.191(3)
R_p	0.0275
R_{wp}	0.0355
R_{exp}	0.0278
R_F	0.0218
R_B	0.0433
χ^2	1.28
Data/restraints/parameter	3802/0/70

[a]The estimated standard deviations were calculated by the Berar's procedure und are indicated in parentheses..

Elemental analysis

The chemical composition of the material was analyzed by CHNS, AAS, and photometry (Table 2). CHNS analysis indicates that the sample contains small amounts of carbon (0.4 ± 0.3 wt%) and hydrogen (0.5 ± 0.3 wt%), which is most likely from decomposition products of the organic ethylene glycol solvent or ascorbic acid reductive because the IR spectrum (see Fig. S3) does not show absorption bands of water. (The estimated amount of water based on the H content would be ~4.5 wt% and would be easily detected by FTIR). Compared to our previous work[8] on olivine $LiCoPO_4$, which used a similar microwave-assisted solvothermal process, it is surprising that no sulfur is detected in the material as $LiCoPO_4$ and Li_2SO_4 are formed during the reaction. The latter one was assumed to form inclusions in the particles that cannot be removed by washing. The fact that the washing step is efficient for the removal of this highly water-soluble side phase in the synthesis of the metastable *Pna*2$_1$-$LiCoPO_4$ might be due to the high surface area of the powder (~60 m^2/g) compared to the olivine (~5.5 m^2/g)[8] and the fact that the particle size is significantly reduced (15 nm *vs.* 700–800 nm × 400–600 nm × 100–220 nm)[8].

Table 2. Elemental analysis of *Pna*2$_1$-$LiCoPO_4$ in comparison with the theoretically expected values[a,b]

Element	a) Theoretical	b) Found
C (wt%)	0	0.4(3)
H (wt%)	0	0.5(3)
Li (wt%)	4.3	3.7(2)
Co (wt%)	36.6	34.8(5)
P (wt%)	19.3	17.4(3)
n(Li):*n*(P)	1	0.95(5)
n(Co):*n*(P)	1	1.05(1)
Empirical formula	$LiCoPO_4$	$Li_{0.95(5)}Co_{1.05(1)}PO_4$

[a]The molar composition is calculated from the experimental values and normalized to the P content (standard deviations in parentheses). [b]The N and S contents were too low to be detected (= 0).

Furthermore, the compound shows a deficit in the absolute Li, Co, and P contents (in wt%) compared to the theoretically expected values. The corresponding Li:Co:P molar ratio of 0.95(5):1.05(1):1.00(2) indicates that the compound is non-stoichiometric, with a deficit in Li and an excess of Co of approximately 5 mol% each, which is in good agreement with the Rietveld refinement results (Table S1). Taking the respective standard deviations into account, these deviations are significant. This is surprising as other reports[10, 12] suggested a stoichiometric 1:1:1 Li:Co:P composition for the compound. Our findings indicate that there is a compositional range, which is probably affected by the synthesis process. Hence, future studies should focus on solid solutions in order to identify the composition range, which could pave the way to tailoring the material properties (*e.g.* by varying the Li:Co:P molar ratios of the starting materials).

Scanning electron microscopy

High-resolution SEM (Fig. 3a) reveals that the as-prepared material consists of uniform, well-crystallized nanospheres with diameters of ~15 nm as expected from the broad reflections observed in the PXRD pattern. Moreover, small agglomerates of ~30–60 nm are observed, which is typical of nanoparticles. The observed particle size is in agreement with the high specific BET surface area of 60.6 ± 0.5 m^2/g, which suggests an average diameter of about 31 nm using Equation 1:

$$d = 6/(S \cdot \rho) \quad (1)$$

with *d* being the particle diameter (m), *S* the specific surface area (kg/m^2), and ρ the density of the material (kg/m^3; here: 3.191 · 10^{-3} kg/m^3 as refined from PXRD data, *cf.* Table 1), and assuming that the particles are spherical and

non-porous. The fact that the diameter derived from BET is slightly bigger than observed from SEM is due to the agglomeration. EDS analysis (Fig. 3b) delivers a composition of 35 ± 1 wt% Co, 17.6 ± 0.4 wt% P, and 48.2 ± 0.7 wt% O, corresponding to a Co:P molar ratio of 1.05(3):1.00(2). The excess of Co is consistent with the results of the elemental analysis (Table 3).

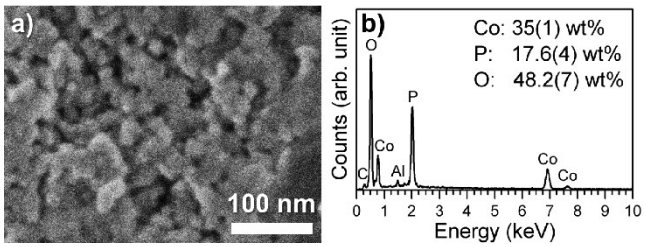

Figure 3. (a) SEM image and (b) corresponding EDS spectrum of the *Pna*2$_1$-LiCoPO$_4$ powder prepared by microwave-assisted solvothermal synthesis. The sample contains spherical nanoparticles with a diameter of ~15 nm. The small C and Al signals observed in the EDS spectrum are from the carbon tape and the aluminum holder used for the measurement.

Synthesis parameters

The formation of the metastable *Pna*2$_1$-LiCoPO$_4$ polymorph strongly depends on the synthesis conditions of the microwave-assisted solvothermal process. Jaehne *et al.*[12] identified the synthesis temperature, pH value, and precursor concentration as key parameters. In our synthesis, however, the solvent composition seems to be a critical factor in obtaining the *Pna*2$_1$ modification. Whereas an aqueous system with 50 vol% ethylene glycol delivers hexagonal platelets of olivine *Pnma*-LiCoPO$_4$ at 250 °C (as shown in our previous work[8]), the metastable *Pna*2$_1$ modification is obtained when pure EG is used. A possible explanation is that diffusion plays an important role in the crystallization of the phases because the boiling points and viscosities of the reaction media differ significantly (EG: 15.7 ± 0.2 mPa•s *vs.* H_2O: 0.89 ± 0.05 mPa•s *vs.* H_2O/EG 1:1 (v:v) mixture: 3.36 ± 0.06 mPa•s measured by rheometry at 25 °C and a shear rate of 100 s^{-1}). As a result, the ion diffusion rates and solubilities of the precursors are reduced in pure EG compared to aqueous solvents, favoring the formation of the metastable product (*Pna*2$_1$-LCP) over the thermodynamic product (*Pnma*-LCP) due to kinetic reaction control. The increased viscosities and slower diffusion rates also affect the particle size, which is significantly reduced compared to our previous work[8] on olivine-type LiCoPO$_4$, because the growth of large crystals is inhibited (Fig. 3). Moreover, EG also acts as a complexing and capping agent, which effectively hinders crystal growth and prevents agglomeration without the need of an additional surfactant.[19]

The formation of *Pna*2$_1$-LiCoPO$_4$, however, is not limited to pure, water-free EG solvents if other parameters are varied. For instance, due to kinetic reaction control, the phase is also accessible by using shorter reaction times (≤ 10 min) in aqueous media (e.g. with 50 vol% EG) while keeping the reaction temperature at 250 °C (not shown). Another option is to decrease the reaction temperature to 200 °C, while keeping the synthesis time at 30 min in order to obtain highly crystalline products. In this case, the metastable phase is obtained for all solvent compositions exclusively, even if pure water is used and highly crystalline, micron-sized particles with cubic and square platelets morphologies are obtained (Fig. S1 and S2, Tables S3–S5). Employing lower temperatures for the process therefore paves the way for the production of various particle sizes and morphologies by changing the solvent composition.

Infrared spectroscopy

The FTIR spectrum of *Pna*2$_1$-LiCoPO$_4$ is shown in the region from 400 cm^{-1} to 1400 cm^{-1} (Fig. 4) and is in good agreement with a previous report[10]. In the region of 1400–4000 cm^{-1} (Fig. S3) no absorption bands of water or other impurities appear, confirming the purity of the material. Generally, the spectrum is expected to be dominated by the four fundamental intramolecular vibrations of the $[PO_4]^{3-}$ tetrahedra, with the frequencies being closely related to the ones of the free molecule (1082 cm^{-1}, 980 cm^{-1}, 515 cm^{-1}, and 365 cm^{-1}).[20] In the spectrum, two main regions can be distinguished: The first region between 400 cm^{-1} and 700 cm^{-1} is associated with the intramolecular $[PO_4]^{3-}$ bending modes (ν_2, ν_4); the region of 900–1200 cm^{-1} corresponds to the intramolecular stretching vibrations (ν_1, ν_3).

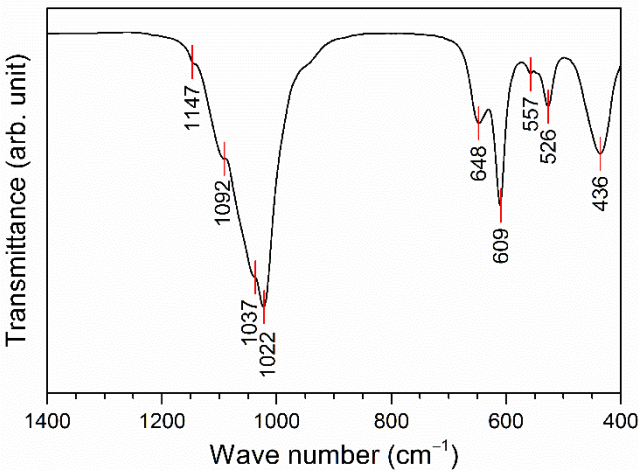

Figure 4. FTIR spectrum of nanosized *Pna*2$_1$-LiCoPO$_4$. The omitted region of 1400–400 cm^{-1} (Fig. S3) does not show any absorption bands of water or other impurities.

More specifically, the bands at 1147 cm^{-1}, 1092 cm^{-1}, and 1037 cm^{-1} are associated with the asymmetric stretching vibrations of P–O (ν_3), which is split up in a triplet due to interactions with the Co–O bonds ($\Delta\tilde{\nu}$ = 55 cm^{-1}). The peaks are significantly broadened as a result of the asymmetric bonding situation in the [PO_4] units in the crystal structure (*cf.* refined interatomic distances, Table S2). In comparison to the spectrum of olivine-type *Pnma*-$LiCoPO_4$,[8] the bands are shifted to lower wavenumbers. This is due to the less covalent character of the P–O bonds, *i.e.* longer P–O distances in the crystal structure (*cf.* Tables S2 and ref.[8]). Surprisingly, the symmetric P–O stretching vibration (ν_1) is not infrared inactive as suggested previously[10] but can be observed at 1022 cm^{-1}. The four bands observed in the region of at 526–648 cm^{-1} are related to antisymmetric O–P–O bending vibrations (ν_4). The absorption at 436 cm^{-1} might be explained by the symmetric bending vibration of O–P–O (ν_2) or a contribution of Li-ion cage modes.[21].

X-ray absorption spectroscopy

The normalized soft XAS Co $L_{2,3}$-edge spectrum of the material in the TEY mode is shown along with CoO and Co_3O_4 powders as reference materials in Fig. 5. Whereas the *L*-edge spectrum of olivine *Pnma*-$LiCoPO_4$ has been reported in our previous work,[8] this is the first time the spectrum of the exclusively tetrahedrally coordinated *Pna*2_1-$LiCoPO_4$ polymorph is presented.

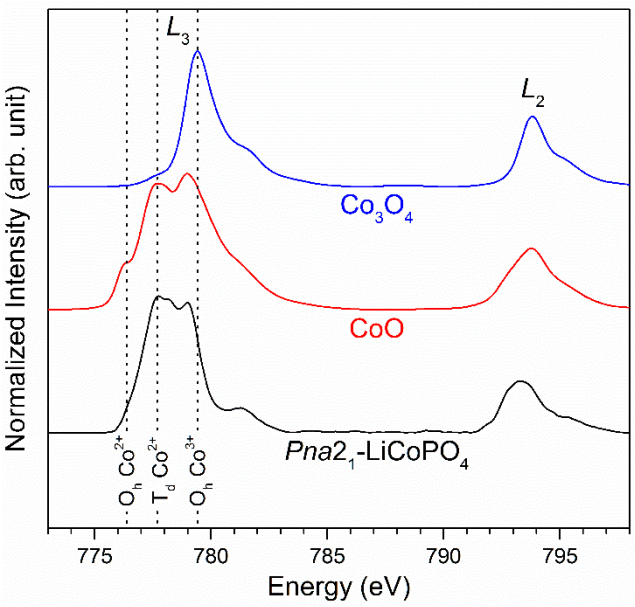

Figure 5. Normalized soft-XAS Co $L_{2,3}$-edge spectra of *Pna*2_1-$LiCoPO_4$ (black) in the TEY detection mode in comparison with CoO (red) and Co_3O_4 (blue) as references. The energies corresponding to O_h Co^{2+} (776.4 eV), T_d Co^{2+} (777.7 eV) and O_h Co^{3+} (779.4 eV) are indicated by dotted lines. It is evident that the sample contains only T_d Co^{2+}.

In general, the absorption peaks of the $L_{2,3}$-edge XAS spectra are highly sensitive to the oxidation state, spin state, and the chemical environment of the transition metal in the crystal. Comparing the main peak at 777.7 eV with the energies of Co^{2+} (777.7 eV) and Co^{3+} (779.4 eV) $L_{2,3}$-edge spectra reported by Hibberd and co-workers[18] and the CoO (which contains O_h Co^{2+}) and Co_3O_4 reference spectra (T_d Co^{2+} and O_h Co^{3+}) shows that the material contains only Co^{2+}. The absence of a low-energy peak at 776.4 eV, which is characteristic for octahedral (O_h) Co^{2+} (*cf.* spectrum of CoO), provides evidence for a tetrahedral (T_d) coordination of Co^{2+} in the structure as expected. The fact that the multiplet structure (caused by electron–electron interactions) is less well-defined than for olivine $LiCoPO_4$ as shown in our previous work[8] is consistent with the fact that the structure is slightly disordered and shows a higher degree of covalence in the [CoO_4] tetrahedra as indicated by the significantly shorter Co–O distances (*cf.* Tables S2 and ref.[8]). Because no shoulder or characteristic peak at 779.5 eV for T_d Co^{3+} is present, it can be inferred that the sample does not contain significant amounts of Co^{3+}. Hence, the ascorbic acid reductant[22] used in the reaction mixture and the weak reducing effect of the ethylene glycol solvent[23] seem to be effectively preventing oxidation of Co^{2+} to Co^{3+} in solution.

Electrochemical characterization

The electrochemical performance of the Pna21 nanospheres was tested in coin cells. . The rate capability and coulombic efficiency were investigated at 0.1 C, 0.5 C, 0.2 C, 1 C, and 2 C for three cycles each (Fig. 6, inset), followed by 20 cycles at 0.1 C (Fig. S4). The galvanostatic curves of the first three cycles at 0.1 C, 0.5 C, and 0.2 C are displayed in Fig. 6. A distinct plateau region at ~4.9 V is only observed in the first charging half cycle. The higher potential compared to olivine $LiCoPO_4$ (~4.8 V[7]) reflects the different coordination of Co in the crystal structures ([CoO_4] *vs.* [CoO_6] units). In the first three cycles at 0.1 C, a discharge capacity of only ~6 mAh/g is reached, corresponding to 4% of the theoretical capacity and significantly lower than previously reported values.[10, 12] Further capacity decrease is observed upon further cycling. The high coulombic inefficiencies indicate that irreversible reactions occur. The nano-morphology should favor rapid diffusion of lithium, so that these results strongly suggest that kinetic effects are not responsible for the poor performance.

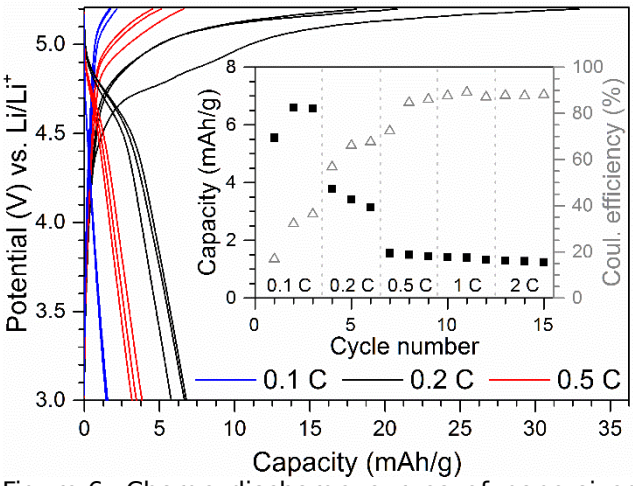

Figure 6. Charge–discharge curves of nano-sized *Pna*2$_1$-$LiCoPO_4$ for the first three cycles at 0.1 C, 0.2 C, and 0.5 C each (the curves for 1 C and 2 C are not shown as the capacities were extremely low). Inset: Specific discharge capacities (■) and coulombic efficiencies (△) *vs.* cycle number for the first 15 cycles at various C rates (average from two cells; error bars are omitted for clarity). Conditions: 3.0–5.2 V, 1 M $LiPF_6$ in EC:DEC (1:1, v:v) at 25 °C.

There are a number of possible reasons for the extremely poor performance, including the low electronic and ionic conductivities of the material, ion-mixing, and the very high potential at which it is electroactive. The observed excess of cobalt results in Li/Co disorder on the Li sites with Co ions blocking diffusion paths, which additionally reduces the conductivity. This could also be the reason for the generally poor performance observed by other groups.[10, 12] Furthermore, decomposition of the electrolyte at the extremely high operating potential seems to play a role,[24] which is exacerbated by the extremely high surface area of the material (~61 m^2/g), as parasitic currents from electrolyte oxidation at high potential are approximately proportional to the BET surface area.[8] Also the influence of residual water in the material (~4.5 wt% derived from TGA and CHNS analysis) may be detrimental to the performance because HF is formed in this case,[25] which leads to metal dissolution or structural decomposition.[26] Another possibility might be structural changes and/or amorphization upon cycling, which will have to be assessed in further experiments. As the performance could not be improved by particle size reduction, future studies should focus on a fundamental understanding of the cycling mechanism, on optimizing the material (reducing metal site mixing) and the electrodes as well as finding electrolytes which are suitable for the potential window (*e.g.* using ionic liquids or additives[27]).

Thermal stability

The thermal stability of the *Pna*2$_1$-$LiCoPO_4$ nanoparticles was assessed by simultaneous TGA/DSC and complementary temperature-dependent *in situ* PXRD measurements performed under air/synthetic air (Fig. 7 and 8). In the TGA curve (Fig. 7), an overall mass loss of ~4.8 wt% is observed, which is due to the removal of residual water (estimated content based on H content found: ~4.5 wt%) as well as to the decomposition of organic residues of the EG solvent and ascorbic acid additive (C content: ~0.4 wt%, see Table 3). The DSC curve shows two signals: a pronounced exothermic peak at 527 °C and a small endothermic signal at 202 °C (Fig. 7, inset). Neither signal is accompanied by a weight loss. The X-ray powder diffraction data of the dark violet sample obtained after the TGA/DSC measurement (Fig. S5, Tables S6–S8) show that phase pure olivine-type *Pnma*-$LiCoPO_4$ was obtained, indicating that one of these signals corresponds to the phase transformation of the *Pna*2$_1$ to the *Pnma* polymorph.

In order to obtain further insights in the processes involved upon heating, the thermal stability was further examined by temperature-controlled *in situ* X-ray powder diffractometry between 30 °C and 900 °C (Fig. 8; zoomed image in the range of 16–29° 2θ see Fig. S6). No phase transitions are observed from 30 °C to 400 °C, indicating that the material is thermally stable up to that temperature. The powder pattern shows a very small shift of the reflections to smaller 2θ values due to thermal expansion, which is evident from the characteristic (210)/(011) reflection (Table S9). Furthermore, the peak width is slightly reduced (Fig. S6) and the intensity of the (210)/(011) reflection increased, indicating that the sample becomes more crystalline. The endothermic signal observed at 202 °C in the DSC might be related to a disorder–order transition, but this cannot be determined from the data. . Between 400 °C and 500 °C, the *Pna*2$_1$-$LiCoPO_4$ transforms to the olivine *Pnma* polymorph. The signal observed in the DSC at 527 °C (Fig. 7) can therefore be assigned to this transition. The lower temperature observed in the *in situ* experiment compared to

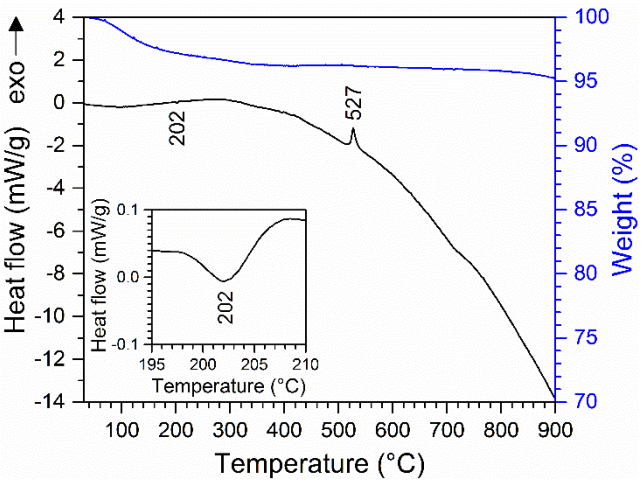

Figure 7. DSC (black) and TGA (blue) curves of *Pna*2$_1$-$LiCoPO_4$ in a temperature range of 30–900 °C (heating rate: 10 °C/min, atmosphere: synthetic air).

An exothermic signal is observed at 527 °C, and an endothermic signal at 202 °C (inset).

the DSC might be because of slightly different atmospheres (air *vs.* synthetic air), and deviating heating rates (10 °C/min *vs.* 5 °C/min) used for the measurements. The phase transformation is not fully complete until 600 °C; traces of the *Pna*2$_1$ phase are still present in the powder pattern at 500 °C as indicated by the (210)/(011) main reflection (not resolved) at ~22.1° 2θ (Fig. S6f). Therefore, the data can still be considered consistent with the TGA/DSC analysis. No further phase changes are observed in the PXRD patterns up to 700 °C. Due to thermal expansion, the reflections are shifted to lower angles, indicating bigger lattice dimensions, and the peak width reduced (Table S9). At 800 °C, the characteristic (210)/(011) reflection of the metastable *Pna*2$_1$ phase reemerges (Fig. S6i), which is in agreement with studies of our group[8] on the thermal stability of *Pnma*-LiCoPO$_4$. This transition, however, is not detected in the DSC experiment. Because the fraction of the *Pna*2$_1$-phase, which is formed, is very low, the heat involved in that process will be very small. Hence, the DSC experiment is probably not sensitive enough to register this transformation. Upon cooling from 900 °C to ambient temperature, the reflections of the *Pna*2$_1$ phase disappear, indicating that the high-temperature transformation is reversible, and pure *Pnma*-LiCoPO$_4$ is obtained, the reflections of which are shifted to higher angles due to thermal contraction. The data here indicate that the transformation to the more stable *Pnma* phase is irreversible. The observation that the phase pure olivine modification is obtained upon heating and cooling thereafter is consistent with our *ex situ* PXRD study (Fig. S5).

The findings of our combined study of the thermal stability differ greatly from previous reports.[10, 12] First of all, the data suggest that not only the transformation of the *Pna*2$_1$ to the *Pnma* polymorph occurs upon heating, but also that a disorder–order transition within the *Pna*2$_1$ structure at lower temperature (202 °C) occurs, and a partial transition of the *Pnma* back to *Pna*2$_1$ structure at very high temperatures (> 800 °C). Unfortunately, it cannot be deduced from our experiment whether the latter transformation is quantitative at even higher temperatures, which will have to be examined in further studies. Secondly, the temperature of 527 °C of the transformation of the *Pna*2$_1$ to the *Pnma* polymorph found in this work is significantly higher than reported values. Jaehne

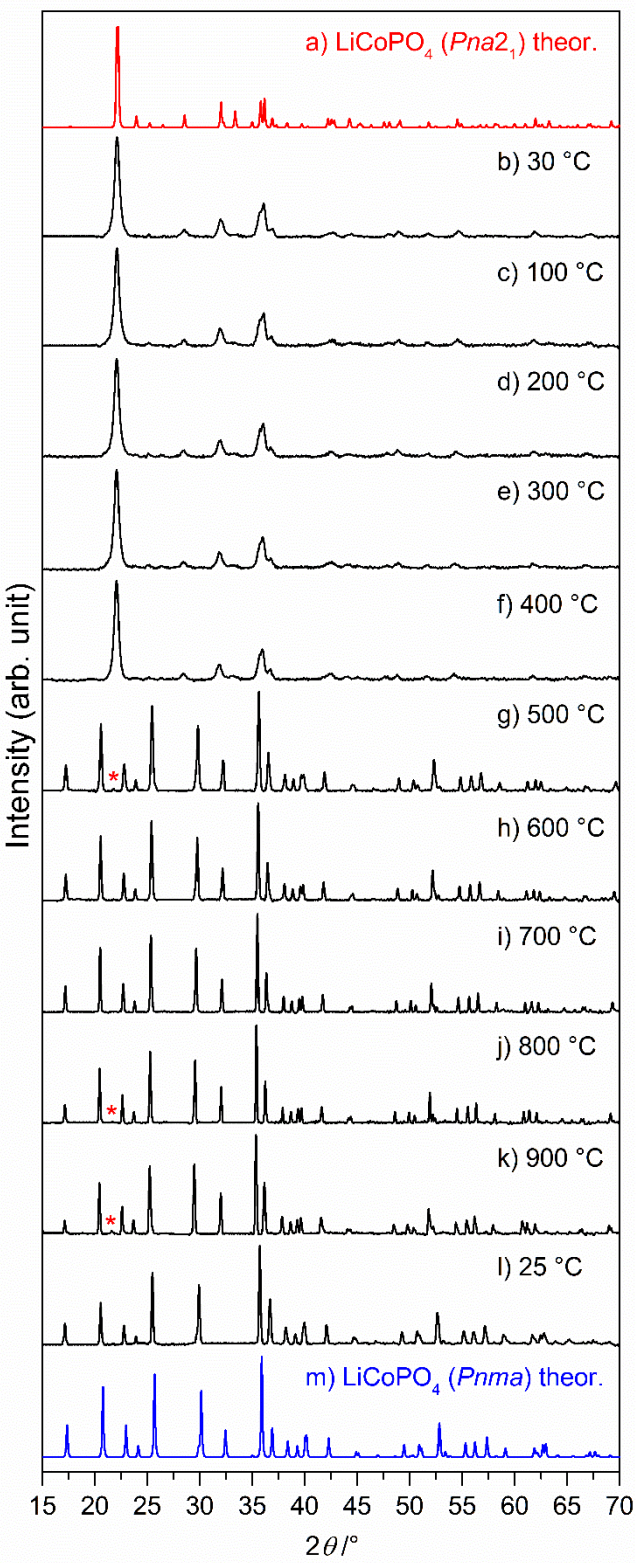

Figure 8. Normalized *in situ* X-ray powder diffraction patterns (Bragg-Brentano geometry, Cu K_α radiation) of nanosized *Pna*2$_1$-LiCoPO$_4$ measured in a range of 30–900 °C (b–k) in air, and after cooling down to 25 °C (l). Between 400 °C and 500 °C, the material starts to transform to the olivine *Pnma*-LiCoPO$_4$ polymorph. At 800 °C, the metastable *Pna*2$_1$ phase reemerges. After cooling, pure *Pnma*-LiCoPO$_4$ is obtained. The theoretical patterns of *Pna*2$_1$- (a) and *Pnma*- LiCoPO$_4$ (m) are displayed in red and blue. The red asterisks (*) in (g, j, k) indicate the

characteristic (210)/(011) reflection of the *Pna*2_1 phase.

et al.[12] reported an exothermic peak at 221 °C (Ar atmosphere, 1 °C/min) while Kreder *et al.* on the other hand, stated that the transition is endothermic and appears at 340 °C (Ar atmosphere, 10 °C/min). The difference is probably related to the heating rates applied as the transformation was also observed at lower temperature when a smaller rate was applied. Also the different atmospheres might play a role. We therefore performed a similar study under an argon stream. The data (DSC/TGA: Fig. S7, S8, Tables S10–S12, *in situ* PXRD: Fig. S9, S10, Table S13) indicate that the atmosphere slightly affects the thermal stability as the phase transition is shifted to higher temperature (580 °C). Another important aspect to explain these differences might be the particle size, with the temperature of the *Pna*2_1–*Pnma* phase transition supposedly increasing with decreasing particle size (*cf.* Jaehne:[12] ~5 μm, Kreder:[10] ~200 nm × 1 μm, this work: ~15 nm). To verify this assumption, we performed a similar study on the micron-sized (~1 μm) material mentioned earlier (Fig. S11–S14, Tables S14–S17). Interestingly, the signal observed in the DSC (Fig. S11), which corresponds to the phase transition of *Pna*2_1- to *Pnma*-$LiCoPO_4$ is significantly lowered to only 163 °C and endothermic instead of exothermic. The lower transition temperature is confirmed by the *in situ* PXRD study (Fig. S13, S14). Our findings therefore indicate that the thermal stability is strongly related to particle size. Nevertheless, the fact that the transition can be either endo- or exothermic (depending on the material) cannot be explained and needs to be investigated in further experiments.

As the *Pna*2_1–*Pnma* phase transformation can be used to produce electrochemically active olivine-type $LiCoPO_4$ by post-annealing,[28] the present work provides a new synthesis pathway towards nanoscaled olivine $LiCoPO_4$. Depending on the particle size, the temperatures can be tremendously lowered compared to the direct solid-state synthesis of the olivine, which requires temperatures above 800 °C.[29] Moreover, as particle size reduction is considered a major strategy to improve the electrochemical performance (rate capability, cycle life) of the olivine[6] but nanoparticles with diameters < 50 nm have only been accessible using high energy-consuming ball-milling steps,[30] this approach could pave the way for an easy and scalable production of the high-voltage cathode material with significant energy savings. In that context, the present work provides fundamental insights which are required for that process.

CONCLUSION

A novel synthesis pathway towards nano-sized particles of the metastable, tetrahedrally coordinated *Pna*2_1-polymorph of $LiCoPO_4$ via a simple and rapid one-step microwave-assisted solvothermal route using ethylene glycol as a solvent was presented. The synthesis yielded nanospheres with diameters of only ~15 nm. The reduced particle dimensions could be related to the high viscosity of the solvent, which inhibits crystal growth and also favors the formation of the metastable phase. In contrast to previous reports, X-ray powder diffraction experiments and elemental analysis indicated that the compound with the empirical sum formula $Li_{0.95}Co_{1.05}PO_4$ is non-stoichiometric and exhibits an excess of cobalt. The approach also allowed for a redetermination of the crystal structure with a disordered cation substructure in which Co ions partially occupies the Li sites. Co $L_{2,3}$-edge X-ray absorption spectroscopic data were reported for the first time, and confirmed the tetrahedral coordination of the Co ions in the structure. The electrochemical performance of the material could not be improved by particle size reduction, with an initial discharge capacity of only 6 mAh/g being reached at 0.1 C. The poor performance could be attributed to the high surface area of the material, which promotes parasitic side reaction, as well as the fact that Li migration is probably hindered due to the structural disorder.

Comprehensive studies on the thermal stability using combined thermogravimetric analysis, differential scanning calorimetry, and temperature-dependent *in situ* X-ray powder diffraction revealed that the material undergoes several phase transformations upon heating. To the best of our knowledge, this complex behavior is reported for the first time. Starting from the *Pna*2_1 phase with a slightly disordered structure, it is assumed that a disorder–order transition occurs at 202 °C. The material then converts to the olivine-type *Pnma* modification at 527 °C, which partly und reversibly transforms back to the initial *Pn*2_1*a* structure. It remained unclear, however, whether the transformation back to the *Pna*2_1 modification is quantitative at temperatures higher than 900 °C, which will have to be investigated in further experiments. After cooling to ambient temperature, a single-phase material of the thermodynamically stable *Pnma* modification was obtained. It was further shown that the temperature of the transformation is significantly affected by the particle size of the material and the atmosphere upon heating.

To sum up, the present work provides new fundamental insights into the structure–property relations of the metastable $LiCoPO_4$ polymorph. The methodology might be applied to investigate other metastable lithium transition-metal phosphates.

ASSOCIATED CONTENT

Supporting Information. 1. Rietveld refinement details of nano-sized *Pna*2_1-$LiCoPO_4$; 2. Structure and morphology of micron-sized *Pna*2_1-$LiCoPO_4$ (SEM/EDS, Rietveld refinement); 3. Full infrared

spectrum of nano-sized *Pna*2_1-$LiCoPO_4$; 4. Electrochemical stability (cycle life) of nano-sized *Pna*2_1-$LiCoPO_4$ at 0.1 C; 5. Investigation of the thermal stability of nano-sized *Pna*2_1-$LiCoPO_4$ under air/synthetic air (Rietveld refinement, zoomed *in situ* PXRD); 6. Investigation of the thermal stability of nano-sized *Pna*2_1-$LiCoPO_4$ under argon (TGA/DSC, Rietveld refinement, *in situ* PXRD); 7. Investigation of the thermal stability of micron-sized *Pna*2_1-$LiCoPO_4$ under air/synthetic air (TGA/DSC, Rietveld refinement, *in situ* PXRD). CSD xxx–xxx (will have to be submitted) contain the crystallographic data for this paper. This material is available free of charge via the Internet at http://pubs.acs.org.

AUTHOR INFORMATION

Corresponding Author

* E-mail: tom.nilges@lrz.tum.de,
Tel.: +49 89 289 13110, Fax: +49 89 289 13762

Author Contributions

J. L. synthesized and characterized the material, and D. N. performed XAS measurements. J. L. wrote the manuscript. All authors participated in the discussion of the results and have given approval to the final version of the manuscript.

Funding Sources

This work has been funded by the Fonds der Chemischen Industrie. The soft XAS experiments were carried out at the Stanford Synchrotron Radiation Lightsource (SSRL), a Directorate of SLAC National Accelerator Laboratory and an Office of Science User Facility operated for the US Department of Energy Office of Science by Stanford University. Use of SSRL, SLAC National Accelerator Laboratory is supported by the US Department of Energy, Office of Science, and Office of Basic Energy Sciences (Contract No. DE-AC02-76SF00515).

ACKNOWLEDGMENT

The authors would like to thank U. Ammari for elemental analysis and K. Rodewald for SEM images. The help of D. Haering with BET and P. Madkikar with TGA/DSC measurements is gratefully acknowledged. J. Ludwig is grateful to the Fonds der Chemischen Industrie for her PhD fellowship.

ABBREVIATIONS

AAS	Atomic absorption spectroscopy
AEY	Auger electron yield
DEC	Diethyl carbonate
DSC	Differential scanning calorimetry
EC	Ethylene carbonate
EDS	Energy-dispersive X-ray spectroscopy
EG	Ethylene glycol
FTIR	Fourier transform infrared spectroscopy
FY	Fluorescence yield
LEI	Lower secondary electron image
NMP	*N*-Methyl-2-pyrrolidone
PVdF	Polyvinylidene difluoride
PXRD	Powder X-ray diffraction
SEM	Scanning electron microscope
TEY	Total electron yield
TGA	Thermogravimetric analysis
XAS	X-ray absorption spectroscopy

REFERENCES

(1) Thackeray, M., Lithium-ion batteries: An unexpected conductor. *Nat Mater* **2002,** 1, (2), 81-82.

(2) Yamada, A.; Hosoya, M.; Chung, S.-C.; Kudo, Y.; Hinokuma, K.; Liu, K.-Y.; Nishi, Y., Olivine-type cathodes: Achievements and problems. *Journal of Power Sources* **2003,** 119–121, (0), 232-238.

(3) Padhi, A. K.; Nanjundaswamy, K. S.; Goodenough, J. B., Phospho-olivines as Positive-Electrode Materials for Rechargeable Lithium Batteries. *J. Electrochem. Soc.* **1997,** 144, (4), 1188-1194.

(4) Okada, S.; Sawa, S.; Egashira, M.; Yamaki, J.; Tabuchi, M.; Kageyama, H.; Konishi, T.; Yoshino, A., Cathode properties of phospho-olivine Li*M*PO_4 for lithium secondary batteries. *J. Power Sources* **2001,** 97-98, 430-432.

(5) Kang, B.; Ceder, G., Battery materials for ultrafast charging and discharging. *Nature* **2009,** 458, (7235), 190-193.

(6) Zaghib, K.; Guerfi, A.; Hovington, P.; Vijh, A.; Trudeau, M.; Mauger, A.; Goodenough, J. B.; Julien, C. M., Review and analysis of nanostructured olivine-based lithium recheargeable batteries: Status and trends. *J. Power Sources* **2013,** 232, 357-369.

(7) Amine, K.; Yasuda, H.; Yamachi, M., Olivine $LiCoPO_4$ as 4.8 V electrode material for lithium batteries. *Electrochem. Solid-State Lett.* **2000,** 3, (4), 178-179.

(8) Ludwig, J.; Marino, C.; Haering, D.; Stinner, C.; Nordlund, D.; Doeff, M. M.; Gasteiger, H. A.; Nilges, T., Facile, ethylene glycol-promoted microwave-assisted solvothermal synthesis of high-performance $LiCoPO_4$ as a high-voltage cathode material for lithium-ion batteries. *RSC Adv.* **2016,** 6, 82984-82994.

(9) Amador, U.; Gallardo-Amores, J. M.; Heymann, G.; Huppertz, H.; Moran, E.; Arroyo-de Dompablo, M. E., High pressure polymorphs of $LiCoPO_4$ and $LiCoAsO_4$. *Solid State Sci.* **2009,** 11, (2), 343-348.

(10) Kreder, K. J.; Assat, G.; Manthiram, A., Microwave-Assisted Solvothermal Synthesis of Three Polymorphs of $LiCoPO_4$ and Their Electrochemical Properties. *Chem. Mater.* **2015,** 27, (16), 5543-5549.

(11) Alarcón-Suesca, C. E.; Ludwig, J.; Hlukhyy, V.; Stinner, C.; Nilges, T., In situ studies and magnetic properties of the *Cmcm*-polymorph of $LiCoPO_4$ with a hierarchical dumbbell-like morphology synthesized by easy single-step polyol synthesis *Inorganics, submitted* **2016**.

(12) Jaehne, C.; Neef, C.; Koo, C.; Meyer, H.-P.; Klingeler, R., A new $LiCoPO_4$ polymorph via low temperature synthesis. *J. Mater. Chem. A* **2013,** 1, (8), 2856-2862.

(13) Petricek, V.; Dusek, M.; Palatinus, L., Crystallographic Computing System JANA2006: General features. *Z. Kristallogr. - Cryst. Mater.* **2014,** 229, (5), 345-352.

(14) Jensen, T. R.; Norby, P.; Stein, P. C.; Bell, A. M. T., Preparation, structure determination and thermal transformation of a new lithium zinc phosphate, δ_I-$LiZnPO_4$. *J. Solid State Chem.* **1995,** 117, (1), 39-47.

(15) Finger, L. W.; Cox, D. E.; Jephcoat, A. P., A correction for powder diffraction peak asymmetry due to axial divergence. *J. Appl. Crystallogr.* **1994,** 27, (6), 892-900.

(16) Berar, J. F.; Lelann, P., E.S.D.'s and estimated probable error obtained in Rietveld refinements with

local correlations. *J. Appl. Crystallogr.* **1991,** 24, (1), 1-5.

(17) Lin, F.; Nordlund, D.; Markus, I. M.; Weng, T.-C.; Xin, H. L.; Doeff, M. M., Profiling the nanoscale gradient in stoichiometric layered cathode particles for lithium-ion batteries. *Energ. Environ. Sci.* **2014,** 7, (9), 3077-3085.

(18) Hibberd, A. M.; Doan, H. Q.; Glass, E. N.; de Groot, F. M. F.; Hill, C. L.; Cuk, T., Co Polyoxometalates and a Co_3O_4 Thin Film Investigated by L-Edge X-ray Absorption Spectroscopy. *J. Phys. Chem. C* **2015,** 119, (8), 4173-4179.

(19) Feldmann, C., Polyol-mediated synthesis of nanoscale functional materials. *Solid State Sci.* **2005,** 7, (7), 868-873.

(20) Herzberg, G., *Infrared and Raman Spectra of Polyatomic Molecules*. Van Nostrand: New York, 1975.

(21) Burba, C. M.; Frech, R., Raman and FTIR spectroscopic study of Li_xFePO_4 ($0 \leq x \leq 1$). *J. Electrochem. Soc.* **2004,** 151, (7), A1032-A1038.

(22) Chen, J.; Vacchio, M. J.; Wang, S.; Chernova, N.; Zavalij, P. Y.; Whittingham, M. S., The hydrothermal synthesis and characterization of olivines and related compounds for electrochemical applications. *Solid State Ionics* **2008,** 178, (31-32), 1676-1693.

(23) Kuppan, S.; Balaya, P.; Reddy, M. V.; Chowdari, B. V. R.; Vittal, J. J., Morphology controlled synthesis of $LiFePO_4$/C nanoplates for Li-ion batteries. *Energy Environ. Sci.* **2010,** 3, (4), 457-464.

(24) Bramnik, N. N.; Bramnik, K. G.; Buhrmester, T.; Baehtz, C.; Ehrenberg, H.; Fuess, H., Electrochemical and structural study of $LiCoPO_4$-based electrodes. *J. Solid State Electrochem.* **2004,** 8, (8), 558-564.

(25) Kawamura, T.; Okada, S.; Yamaki, J.-i., Decomposition reaction of LiPF6-based electrolytes for lithium ion cells. *J. Power Sources* **2006,** 156, (2), 547-554.

(26) Markevich, E.; Sharabi, R.; Gottlieb, H.; Borgel, V.; Fridman, K.; Salitra, G.; Aurbach, D.; Semrau, G.; Schmidt, M. A.; Schall, N.; Bruenig, C., Reasons for capacity fading of $LiCoPO_4$ cathodes in $LiPF_6$ containing electrolyte solutions. *Electrochem. Commun.* **2012,** 15, (1), 22-25.

(27) Sharabi, R.; Markevich, E.; Fridman, K.; Gershinsky, G.; Salitra, G.; Aurbach, D.; Semrau, G.; Schmidt, M. A.; Schall, N.; Bruenig, C., Electrolyte solution for the improved cycling performance of $LiCoPO_4$/C composite cathodes. *Electrochem. Commun.* **2013,** 28, 20-23.

(28) Neef, C.; Meyer, H.-P.; Klingeler, R., Morphology-controlled two-step synthesis and electrochemical studies on hierarchically structured $LiCoPO_4$. *Solid State Sci.* **2015,** 48, 270-277.

(29) Jang, I. C.; Lim, H. H.; Lee, S. B.; Karthikeyan, K.; Aravindan, V.; Kang, K. S.; Yoon, W. S.; Cho, W. I.; Lee, Y. S., Preparation of $LiCoPO_4$ and $LiFePO_4$ coated $LiCoPO_4$ with improved battery performance. *J. Alloys Compd.* **2010,** 497, (1-2), 321-324.

(30) Rabanal, M. E.; Gutierrez, M. C.; Garcia-Alvarado, F.; Gonzalo, E. C.; Arroyo-de Dompablo, M. E., Improved electrode characteristics of olivine-$LiCoPO_4$ processed by high energy milling. *J. Power Sources* **2006,** 160, (1), 523-528.

Table of Contents